buildings

MDPI

Article

Internal Damping Ratio of Normal- and High-Strength Concrete Considering Mechanical Damage Evolution

Gustavo de Miranda Saleme Gidrão [1,*], Pablo Augusto Krahl [2], Rúbia Mara Bosse [1], Laura Silvestro [1], Rodrigo S. Ribeiro [1], Geannina Terezinha dos Santos Lima [3] and Ricardo Carrazedo [4]

[1] PPGEC-PB/PPGEC-CT/COECI-GP, Universidade Tecnológica Federal do Paraná, Av. Guarapuava, 800-Cidade dos Lagos, Guarapuava 85053-525, PR, Brazil; rubiambosse@utfpr.edu.br (R.M.B.); laurasilvestro@utfpr.edu.br (L.S.); rodrigosribeiro@utfpr.edu.br (R.S.R.)
[2] Departamento de Engenharia Civil, Universidade Presbiteriana Mackenzie, Av. Brasil, 1.220, Jd. Guanabara, Campinas 13073-148, SP, Brazil; pablo.krahl@mackenzie.br
[3] Programa Pesquisa Produtividade do Centro Universitário Estácio, R. Santo Antônio, s/n - Barreiros, São José 88117-350, SC, Brazil; geanninasantos@hotmail.com
[4] Departamento de Estruturas EESC—SET, Escola de Engenharia de São Carlos, Universidade de São Paulo, Avenida Trabalhador São-Carlense, 400-Parque Arnold Schimidt, São Carlos 13566-590, SP, Brazil; carrazedo@sc.usp.br
* Correspondence: gidrao@utfpr.edu.br

Abstract: This paper significantly extends investigations into internal damping ratios in both undamaged and damaged conditions for normal-strength concretes (NSCs) and high-strength concretes (HSCs). This study examines concretes with compressive strengths ranging from 42 to 83 MPa. Cyclic loads were applied using a servo-controlled hydraulic testing machine, and for each cyclic step, the dynamic elastic modulus (E_d) and internal damping ratio (ξ) were determined through acoustic tests. The results show that the normal-strength concretes ($f_c = 42$ MPa) exhibited an undamaged internal damping ratio of $\xi = 0.5\%$, reaching a maximum of $\xi = 2.5\%$ at a damage index of 0.8. Conversely, the high-strength concrete mixtures ($f_c = 83$ MPa) showed an undamaged internal damping ratio of $\xi = 0.29\%$, with a peak value of $\xi = 0.93\%$ at a damage index of 0.32. The initial internal damping values are influenced by porosity and transition zones, which affect the material behavior under cyclic loads. Progressive damage leads to increased Coulomb damping due the cracking process. Few studies have quantified and comprehended the internal damping ratio under cyclic loading-induced damage, and this research advances our understanding of NSC and HSC behavior under dynamic excitation and damage evolution, especially in impact scenarios.

Keywords: internal damping ratio; acoustic tests; usual concretes; damage evolution; high-strength concretes

check for updates

Citation: Gidrão, G.d.M.S.; Krahl, P.A.; Bosse, R.M.; Silvestro, L.; Ribeiro, R.S.; Lima, G.T.d.S.; Carrazedo, R. Internal Damping Ratio of Normal- and High-Strength Concrete Considering Mechanical Damage Evolution. *Buildings* **2024**, *14*, 2446. https://doi.org/10.3390/buildings14082446

Academic Editor: Bo-Tao Huang

Received: 12 June 2024
Revised: 15 July 2024
Accepted: 24 July 2024
Published: 8 August 2024

1. Introduction

The internal damping ratio (ξ) is a dimensionless metric that measures a material's capability to dissipate vibrational energy [1,2]. This parameter is vital for evaluating seismic performance and monitoring the structural health of materials [3]. A time domain technique for identifying damping properties has been presented, which utilizes either a refined linear model or a nonlinear energy-dissipating constitutive model to accurately depict energy dissipation mechanisms such as cracking and friction in reinforced concrete (RC) structures [4–8].

As noted by Bachmann [5], the value of ξ for standard concretes with little to no damage falls within the range of 0.1% to 1.0%. This internal damping ratio, essential for modeling structural dynamics through numerical simulations, is also critical in characterizing the material's internal response to thermal shock [9,10]. Evaluating this ratio enables the assessment of concrete structure degradation [11,12].

The material's internal damping ratio comprises hysteretic, viscous, and Coulomb components [13,14]. Hysteretic damping stems from microstructural sliding friction [15,16], viscous damping results from the presence of moisture within the cement matrix [15,17,18], and the Coulomb component is due to friction between crack surfaces. Of these, Coulomb damping is the predominant mechanism influencing the concrete's internal damping ratio [4,13,14,19,20].

Microstructural features such as porosity, the transition zone, and existing microcracks have a significant correlation with the internal damping ratio. For example, reducing the water–cement ratio minimizes porosity, the transition zone, and microcracks, thereby increasing the material's strength [21]. As the material's density rises, acoustic waves transmit more effectively, resulting in a lower internal damping ratio [22–25].

On the other hand, when the structural integrity of the material is compromised and it shows numerous cracks and porosity, it reduces the acoustic signal [25,26]. This phenomenon occurs at different scales, influencing pastes, mortars, conventional concretes [23,27,28], and UHPFRCs [25], thereby impacting ξ.

When subjected to compressive strains, cracks are already present in the interfacial transition zone (ITZ) and begin to propagate through the interfaces of the aggregate matrix, as well as air voids and pores. The induction of mechanical damage in the samples leads to greater attenuation due to the formation of discontinuities, which enhances the material's ability to dissipate kinetic energy through friction between newly created crack surfaces. Consequently, the damping of the material is linked to the damage mechanisms that occur under severe loading conditions and pre-existing cracks [25].

Recent progress has been made in understanding the internal damping ratio of concretes [29–33]. Tian et al. [30] examined the impact of rubber powder on the internal damping capacity of polypropylene fiber-reinforced concrete (PFRC), discovering that rubber powder enhances the damping capacity of PFRC. Additionally, Tian et al. [29] investigated the use of damping aggregate (DA) in new cement mortar, finding that the damping ratio of samples with 70% DA was nearly three times higher than that of the reference mortar, with a slight reduction in mechanical properties.

The link between the damage index and the internal damping ratio is not well understood for both conventional and high-strength concretes. Therefore, this article builds on the work of Gidrão et al. [25] and explores the internal damping ratio of typical and high-strength concretes (ranging from 42 MPa to 83 MPa), when exposed to cyclic mechanical loads. The findings help to elucidate the behavior of the internal damping ratio in relation to mix parameters and damage progression for different types of concrete and could inform dynamic damping models that account for damage evolution.

2. Experimental Program

2.1. Materials and Mixtures

Table 1 presents the proportion (in weight) of the concrete mixtures produced. The relation of the cement aggregates was equal to 5 (mix proportions of 1 cement–2 sand–3 coarse aggregate). The water–cement relationship (w/c) was modified to 0.3 to 0.7. Ten specimens were produced for each mixture of concrete. The cement used was ordinary Portland type III cement specified according to the classification of ASTM C150 [34], with 3.10 g/cm^3 density. The sand used was classified as zone 1, with a maximum diameter of 0.60 mm, a fineness modulus of 1.74 [35], and a density of 2.65 g/cm^3. The coarse aggregate used was with maximum diameters equal to 9.5 mm and density equal to 2.75 g/cm^3, all produced by diabasic rocks, classified as igneous. The grading curves for the sand and coarse aggregate are shown in Figure 1a and 1b, respectively. The superplasticizer used in the mixture with w/c = 0.3 was Glenium 51, produced by BASF®, produced in São Bernardo Brazil.

The production of concrete samples consisted of (i) mixing cement and aggregates without water addition, then (ii) water was added and the mixing procedure was carried out until the material showed a homogeneous appearance, and (iii) after hardening, the molds were removed and immediately stored in a moist chamber for curing until it was time for testing. Five cylindrical samples of 200 mm height × 100 mm diameter were produced for each mixture, following the ASTM C215 code [36].

Table 1. Concrete mixtures.

ID	w/c (kg/kg)	Cement (kg/kg)	Sand (kg/kg)	Aggregate (kg/kg)	d_{max} (mm)	SP. (% in Cement Mass)
1	0.7	1	2	3	9.5	0
2	0.5	1	2	3	9.5	0
3	0.3	1	2	3	9.5	2

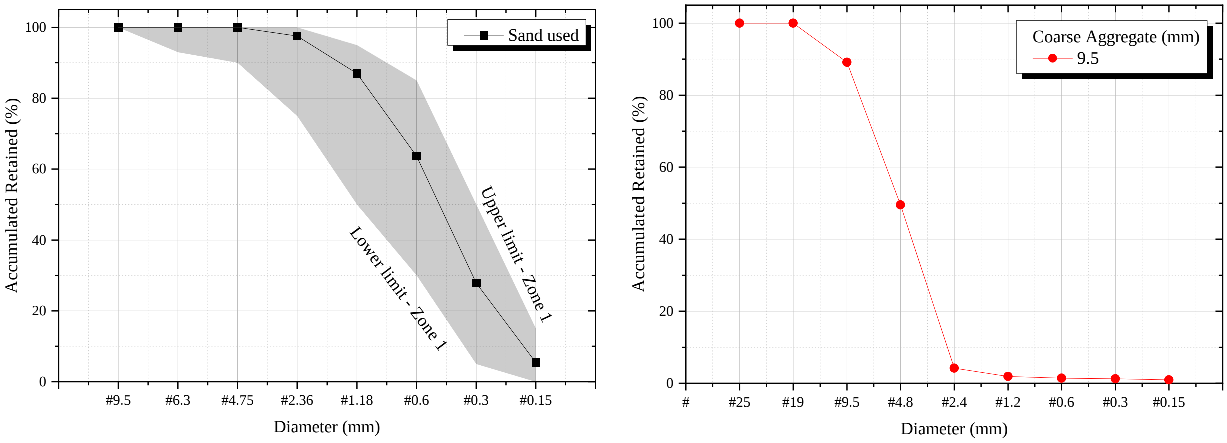

(**a**) Sand (**b**) Coarse aggregate

Figure 1. Material characteristics.

2.2. Cyclic Tests

Cyclic tests were performed systematically to failure using a servo-controlled hydraulic testing machine (Figure 2) at a constant force rate of 2.4 kN/s. Initially, the applied criterion involved loading until a predefined stress level was reached, usually 50%, 60%, 70%, 80%, 90%, and 95% of f_c. At the end of each cycle, an acoustic test was performed to measure the dynamic elastic modulus ($E_{d,i}$), damage index (D_i), and internal damping ratio. Figure 2 depicts the setup for the cyclic tests, while Figure 3 illustrates the characteristic force–displacement diagram for the concretes produced.

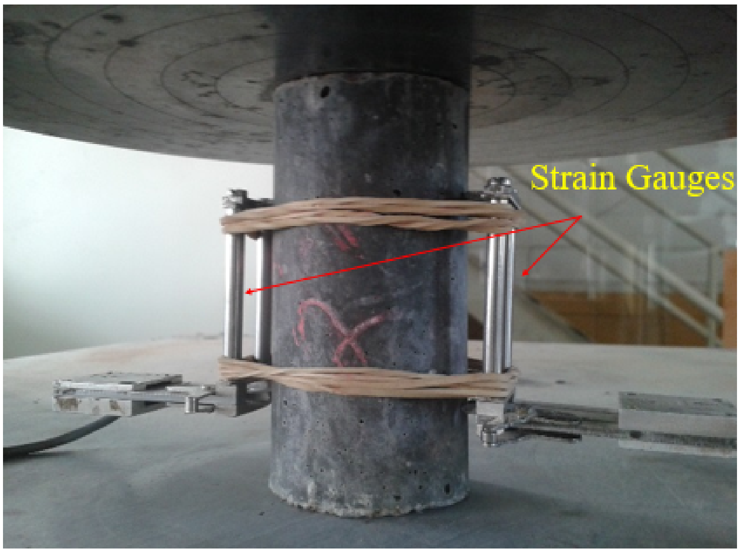

Figure 2. Cyclic test setup.

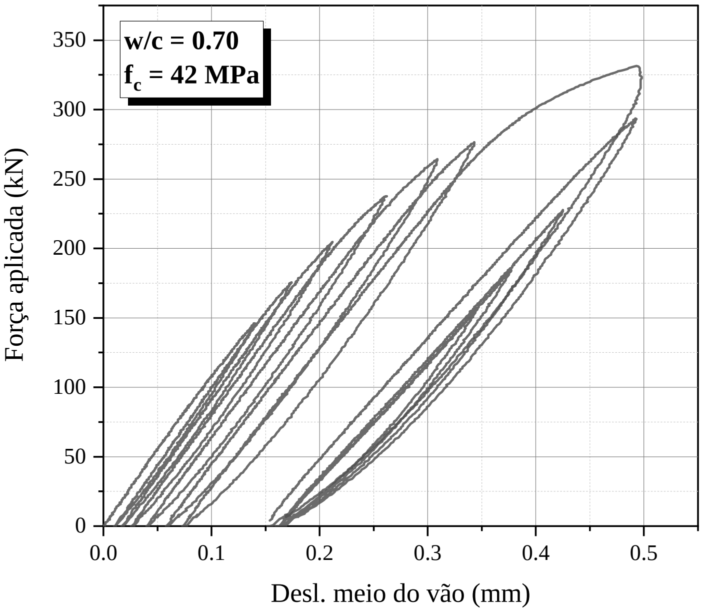

Figure 3. Characteristic force–displacement diagram.

2.3. Acoustic Tests

After each cycle ended, acoustic evaluations (Figure 4a) were performed to assess damage indices and internal damping ratio. The testing method is described by ASTM C215-02 (2003) [36] and ASTM E1876-01 (2001) [37], and involves the use of a hammer to apply brief manual excitation to samples. A one-dimensional microphone recorded the amplitude of the acoustic response in the time domain. An onboard sound card from a standard notebook captured the acoustic signal at a sampling rate of 96 kHz. Subsequently, this signal was processed by the Sonelastic® 6.0 software.

Initially, the software employs a 1024-point block and multiplies the signal by a flat-top window function. This is followed by zero-padding to transform it into an 8192-point vector. By applying a Fast Fourier Transform (FFT), the signal is converted from the time domain to the frequency domain, allowing for the identification of natural frequency peaks. When an eccentric impact excites the sample, the frequency peaks and modes of vibration resemble those shown in Figure 4. It is important to highlight that the vibration modes of the cylinder depicted in Figure 4b were derived from a numerical model using Abaqus 6.14® software. This preliminary analysis facilitated the determination of natural frequencies and vibration modes through eigenvalue analysis.

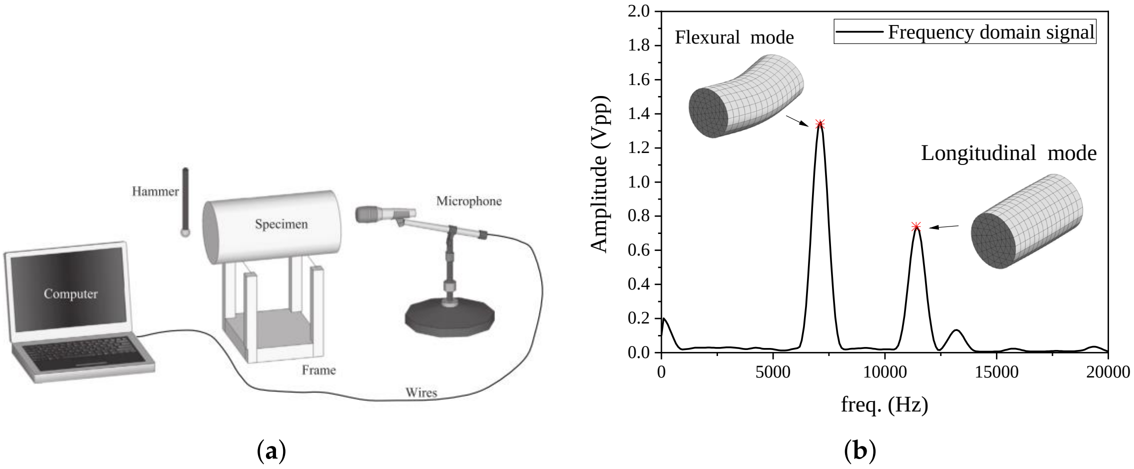

(**a**) (**b**)

Figure 4. Acoustic test. (**a**) Acoustic test; (**b**) FFT signal (adapted from [25,38,39]).

In this FEM analysis, the C3D8R element type was employed with a total of 1000 finite elements represented. The model did not include distortional control. To acquire the characteristic natural frequency for estimating signal localization, a linear elastic, isotropic model with a constant density was implemented. The boundary condition was free–free. Additional details about this approach can be found in Haach et al. [40]. As per ASTM C215-02 (2003) [36], the dynamic elastic modulus (E_d) for cylindrical concrete specimens can be determined by the first longitudinal mode (Equations (1) and (2)) and the first flexural mode (Equations (3) and (4)).

$$E_{d,long} = DM(f_{1,L})^2 \tag{1}$$

$$D = 5.093\frac{L}{d^2} \tag{2}$$

$$E_{d,flex} = CM(f_{1,F})^2 \tag{3}$$

$$C = 1.6067\frac{LT}{d^2} \tag{4}$$

where M is the mass of the sample (in kilograms), L and d are the length and diameter of the sample (in meters), respectively, $f_{1,L}$ is the frequency of the longitudinal vibration mode (Hz), $f_{1,F}$ is the frequency of flexural vibration mode (Hz), and T is a correction factor. The correction factor was derived by Pickett [41] and presented in Equation (5).

$$T = 1 + 4.939(1 + 0.0752\mu + 0.8109\mu^2)\left(\frac{d}{L}\right)^2 - 0.4883\left(\frac{d}{L}\right)^4 - \left[\frac{4.691(1 + 0.2023\mu + 2.173\mu^2)\left(\frac{d}{L}\right)^4}{1 + 4.754(1 + 0.1408\mu + 1.536\mu^2)\left(\frac{d}{L}\right)^2}\right] \tag{5}$$

where μ is the Poisson ratio, assumed as 0.20.

The damage index D_i is obtained with Equation (6):

$$D = 1 - \frac{E_{d,i}}{E_{d,0}} \tag{6}$$

where $E_{d,i}$ is the dynamic elastic modulus at the i-th cycle and $E_{d,0}$ is the dynamic elastic modulus for the undamaged condition.

Additionally, for every peak in natural frequency, the software aligns individual curves depicting the progression of amplitude for each frequency noted in the time frequency matrix and subsequently determines the internal damping ratio ξ as per Equation (7) (also refer to Figure 5). The curve alignment utilizes the Levenberg–Marquardt algorithm [42,43], a computational method that prioritizes regions by fine-tuning the amplitude function based on experimental data. Internal damping ratios were derived for both flexural and longitudinal frequency peaks. For the analysis in this paper, the longitudinal internal damping ratio was emphasized due to the precision of this specific vibration mode.

$$\xi = \frac{1}{2\pi m} ln\left(\frac{x_n}{x_{n+m}}\right) \tag{7}$$

where x_n and x_{m+n} are consecutive amplitudes considered on the analysis, as shown in Figure 5; m is the number of peaks between amplitudes.

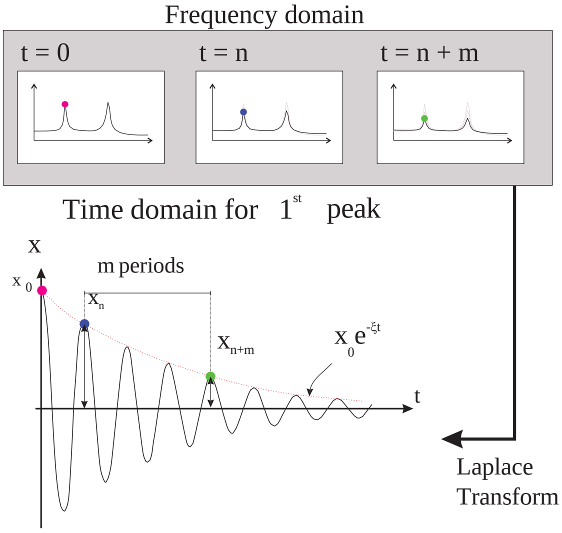

Figure 5. Damping determination (adapted from [25]).

3. Results

Acoustic tests were performed in undamaged samples with the aim of determining the influence of time maturity, the water cement ratio, and the dynamic elastic modulus on the internal damping ratio in Section 3.2. After 28 days, the internal damping ratio became stable, and then cyclic loading was performed to achieve the evolution of the damage, material degradation, and observation of the internal damping ratio, and this is presented in Section 3.3. Section 3.1 presents the uniaxial strength of the developed mixtures.

3.1. Uniaxial Compressive Strength

Figure 6 shows the compressive strength (f_c) of the conventional concrete mixes with different water–cement (w/c) ratios: 0.7, 0.5, and 0.3, at 28 days. Each box plot shows the mean compressive strength (indicated by a square), the median (horizontal line), the standard deviation (box height), and the range within 1.5 times the interquartile range (IQR—whiskers). In addition, individual test points are marked to highlight variability in the data.

The concrete mix with a w/c ratio of 0.7 has the lowest compressive strength, with values of around 40 MPa, showing relatively little variability. The mix with a w/c ratio of 0.5 has a higher compressive strength, around 60 MPa, with a moderate range of variability. The highest compressive strength is observed in the 0.3 w/c mix, reaching around 75 MPa, although it has a wider range of variability compared to the other mixes.

The results of the ANOVA analysis indicate statistically significant differences in the compressive strengths among the different water-to-cement (w/c) ratios, according to Table 2. The comparison between the concrete mixes with w/c = 0.7 and w/c = 0.5 resulted in an F-value of 222.55 and a p value of 4.52×10^{-9}, indicating a significant difference. Similarly, the comparison between the concrete mixes with w/c = 0.7 and w/c = 0.3 showed an F-value of 1267.10 and a p-value of 3.32×10^{-12}, also demonstrating a statistically significant difference. Finally, the comparison between w/c = 0.5 and w/c = 0.3 yielded an F-value of 109.60 and a p-value of 1.95×10^{-7}, confirming the presence of a significant difference. These results suggest that the variation in the water-to-cement ratio has a substantial impact on the compressive strength of concrete, emphasizing the importance of optimizing this ratio to achieve the desired properties of the material.

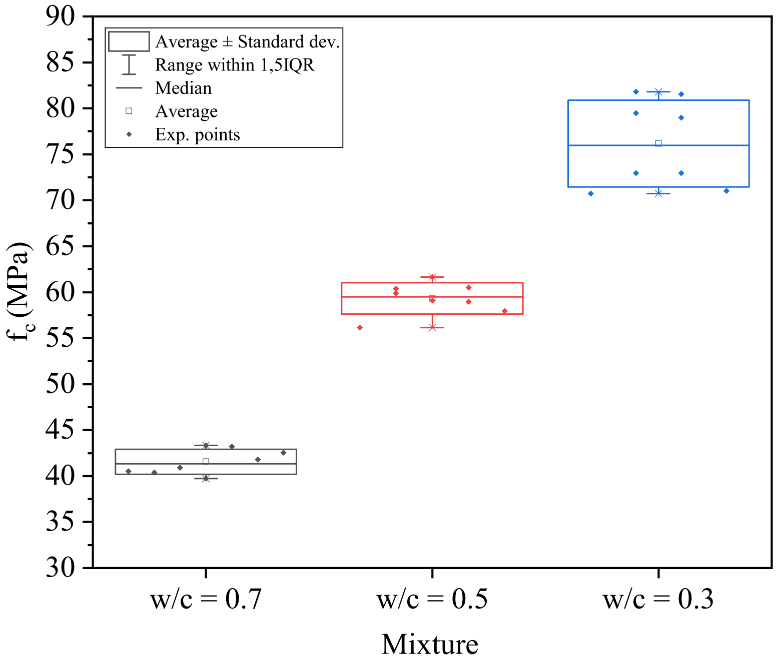

Figure 6. Compressive strength—28 days.

Table 2. ANOVA results for different water-to-cement ratios.

Comparison	F-Value	*p*-Value	Significance
w/c = 0.7 vs w/c = 0.5	222.55	4.52×10^{-9}	Significant difference
w/c = 0.7 vs w/c = 0.3	1267.10	3.32×10^{-12}	Significant difference
w/c = 0.5 vs w/c = 0.3	109.60	1.95×10^{-7}	Significant difference

3.2. Undamaged Samples

Figures 7–10 show the behavior of the internal damping ratio and dynamic elastic modulus (E_d) as a function of maturity for the concretes with w/c = 0.3, 0.5, and 0.7, respectively. Internal damping presents a decrease over the first 5 days for concretes with w/c = 0.5 and 0.7, and the next ξ becomes stable, until 28 days have passed. For the samples with w/c = 0.7, a decrease in ξ is observed until 15 days have passed, probably due to its ITZ. These results are strongly related to the microstructure that develops early on. When concrete hardens, there is a loss of water, the chemical transformation of anhydrous cement to CSH, and the formation of transition zones. Water loss generates a decrease in the internal damping ratio due to the viscous damping parcel. In addition, the increase in the C-S-H concentration improves the density of the microstructure, closes the pores, and reduces the the material's imperfection. The previously described microcracks in the transition zone are also responsible for the Coulomb parcel of the damping, and their connection is linked to the water–cement ratio and coarse aggregate size. Consequently, there is a decrease in ξ and an increase in E_d, according to the observed results in Figures 7–9. The decrease in internal damping over time is more marked in mixtures with a w/c equal to 0.7, followed by those with w/c = 0.5 and w/c = 0.3. Hence, the water–cement ratio and porosity level influences this decrease, and can be observed in Figures 7–9, The mixture with a high level of porosity (i.e., w/c = 0.7) departs a high level of internal damping ($\xi = 0.8$) and decreases until 15 days have passed due the high occurrence of pores, voids, and previously formed microcracks.In the mixtures with minor porosity and previously formed microcracks (that is, w/c = 0.3 and 0.7), the decrease in the internal damping ratio is faster. Hence, the scale of porosity and the transition zone severely influences the material's internal damping ratio, and this microstructure will be important for explaining the behavior of the material under mechanical cycles, as is presented in Section 3.3.

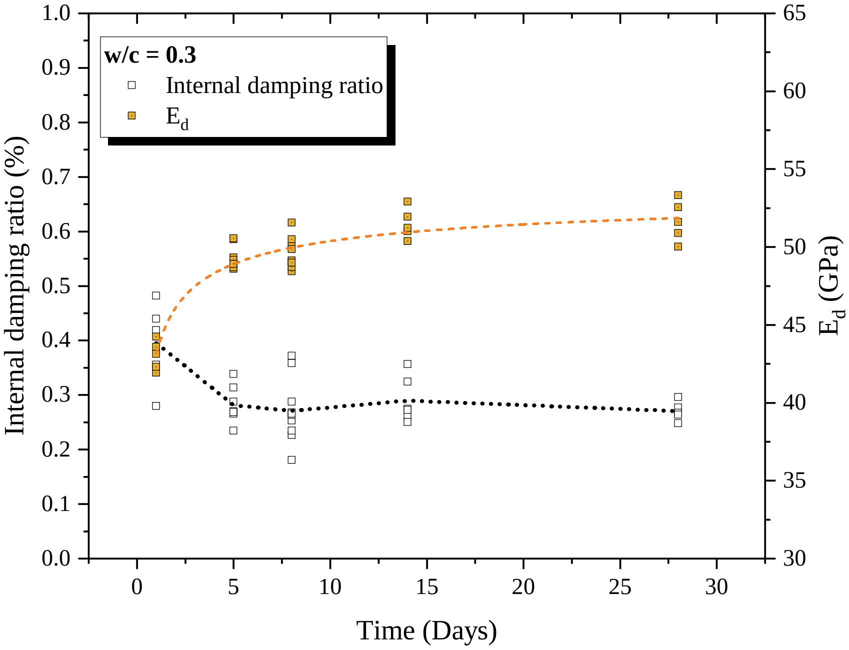

Figure 7. Internal damping ratio and dynamic elastic modulus over time—w/c = 0.3.

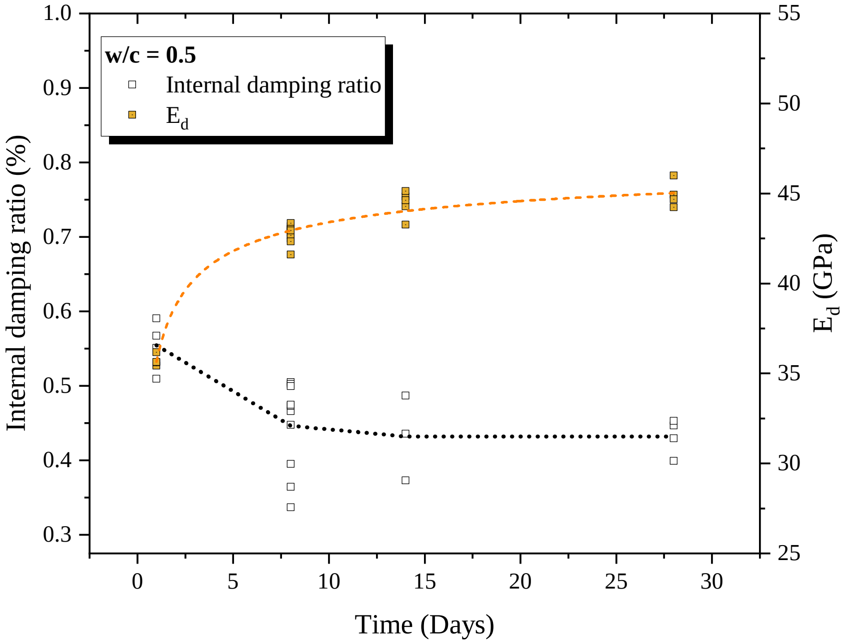

Figure 8. Internal damping ratio and dynamic elastic modulus over time—w/c = 0.5.

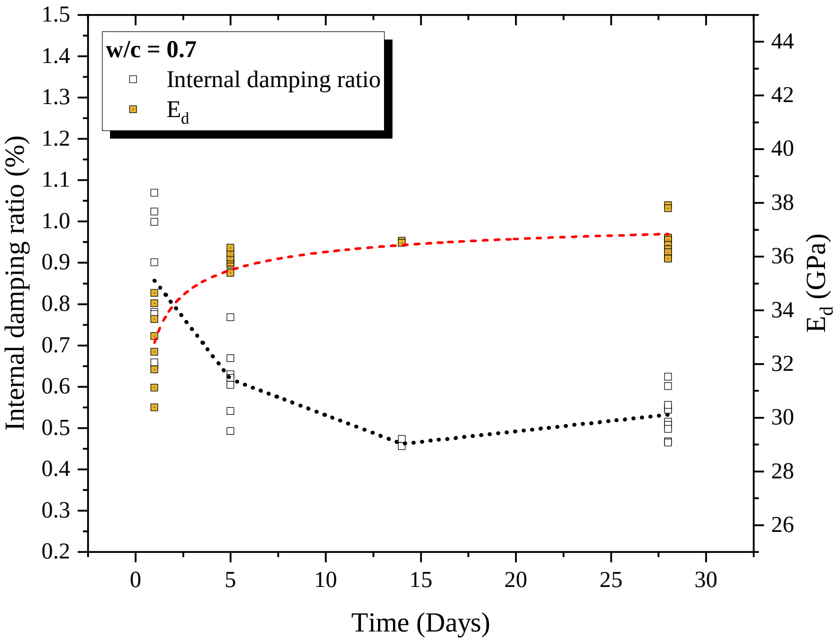

Figure 9. Internal damping ratio and dynamic elastic modulus over time—w/c = 0.7.

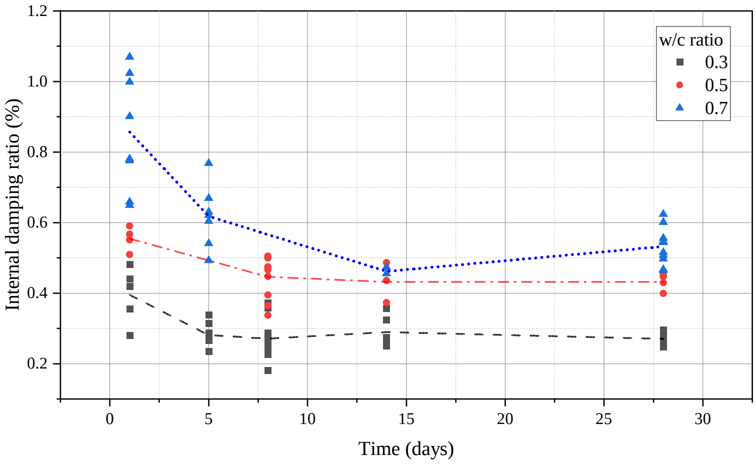

Figure 10. Internal damping ratio over time with different w/c.

An empirical relation of E_d and ξ could be presented according to Figure 11. Equation (8) was used to calibrate the experimental data, with $a = 0.673$, $b = -0.0317$ and $c = -1.26 \times 10^{-4}$, with $R^2 = 0.800$. Despite the large variability, there is a clearly downward trend between these parameters, confirming that the internal damping ratio is correlated with the occurrence of microstructure imperfections, such as voids, porosity, and transition zones, factors which influence E_d negatively. In particular, the internal damping ratio shows a greater statistical dispersion compared to the dynamic elastic modulus, and is mainly influenced by factors such as moisture content and the level of manual impacts applied during testing. However, the trend is clear: the internal damping ratio decreases as the material quality increases.

$$\xi = e^{a+b.E_d+cE_d^2} \tag{8}$$

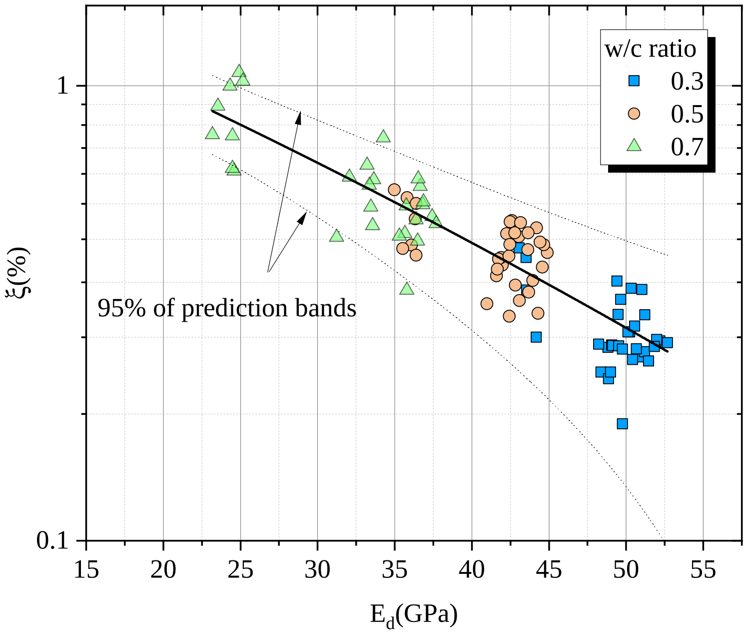

Figure 11. Internal damping ratio and E_d.

Figure 12 shows the comparison of the internal damping ratio between the conventional concrete (NSC—1:2:3 with w/c ratios of 0.5 and 0.7) and high-strength concrete (HSC—1:2:3 with a w/c ratio of 0.3) for intact samples at 28 days. As observed in Figure 12, an increase in the w/c ratio systematically improves the level of pre-existing microcracks and the interfacial transition zone (ITZ), which subsequently increases the dissipation of acoustic waves. This process deteriorates the quality of the signal and improves the internal damping ratio [25].

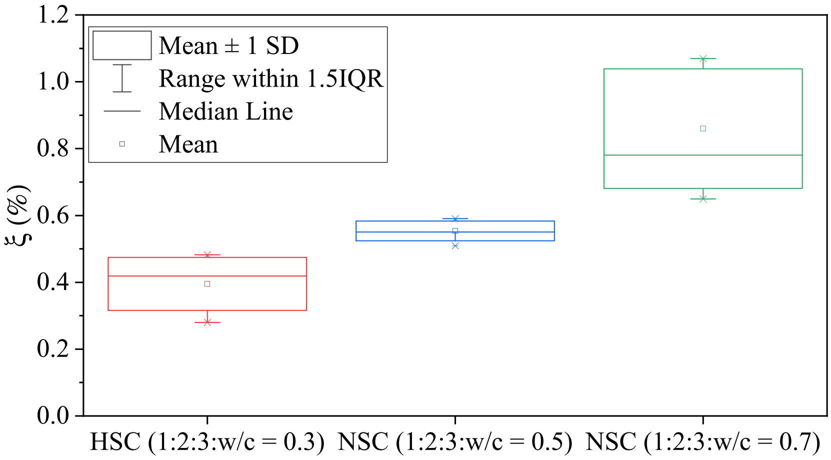

Figure 12. Comparison of mixtures.

The ANOVA results in Table 3 indicate statistically significant differences between the concrete mixtures with different water-to-cement (w/c) ratios. The comparison between concretes with w/c = 0.7 and w/c = 0.5 showed an F-value of 21.18 and a p value of 3.7×10^{-5}, suggesting a significant difference between these two mixtures. Similarly, the comparison between w/c = 0.7 and w/c = 0.3 resulted in an F-value of 39.17 and a p value of 2.4×10^{-6}, confirming the presence of significant differences. Finally, the comparison between the concreted with w/c = 0.5 and w/c = 0.3 presented an F-value of 33.13 and a p value of 6.2×10^{-6}, also indicating a statistically significant difference.

Table 3. ANOVA results.

Comparison	F-Value	p Value	Interpretation
w/c = 0.7 vs w/c = 0.5	21.18	3.7×10^{-5}	Significant difference
w/c = 0.7 vs w/c = 0.3	39.17	2.4×10^{-6}	Significant difference
w/c = 0.5 vs w/c = 0.3	33.13	6.2×10^{-6}	Significant difference

3.3. Damaged Samples

Figure 13a–c show a typical stress–strain relationship for the blends studied. It is interesting to note that hysteretic behavior was observed during cyclic loading. The area within the load–reload–strain curves can be described as hysteretic. Damping [1,25] and the increase in this area over the cycles represents the increase in energy dissipation and therefore internal damping of the material. There is visible low hysteretic damping at w/c = 0.3 and a high hysteretic damping at w/c = 0.5 and 0.7 due the above mentioned microstructural characteristics. The figure presented here, Figure 6, shows a box plot that contains the maximum compressive stress for the assessed concretes.

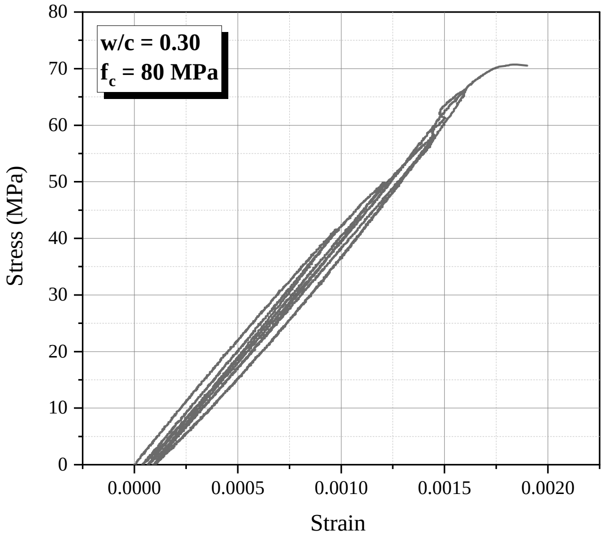

(**a**) w/c = 0.3

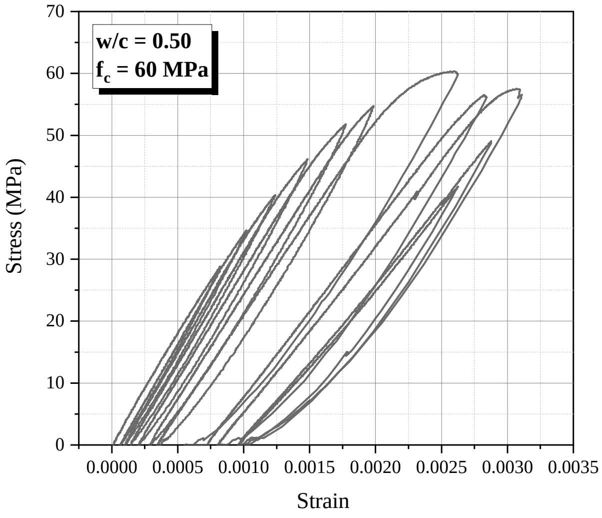

(**b**) w/c = 0.5

Figure 13. *Cont.*

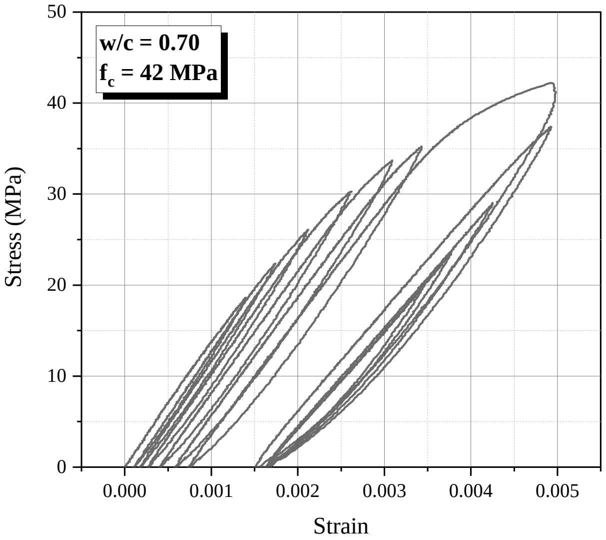

(**c**) w/c = 0.7

Figure 13. Typical stress–strain diagram.

Figures 14–16 illustrate the progression of the damage index (D_i) in relation to the nondimensional stress—a parameter derived from the ratio of the maximum stress during the cycle (σ_i) to the peak strength of the specimen (f_c). These figures depict the anticipated damage evolution over the cycles. The mixtures with w/c ratios of 0.5 and 0.7 exhibit significant damage at the point of fracture, whereas the 0.3 water–cement mixture shows a fragility level reaching a damage index of 0.35. Notably, there is potential for using acoustic testing to evaluate the damage index in the concrete samples.

Figures 17–19 display the resulting relationship between the internal damping ratio and the progression of damage.

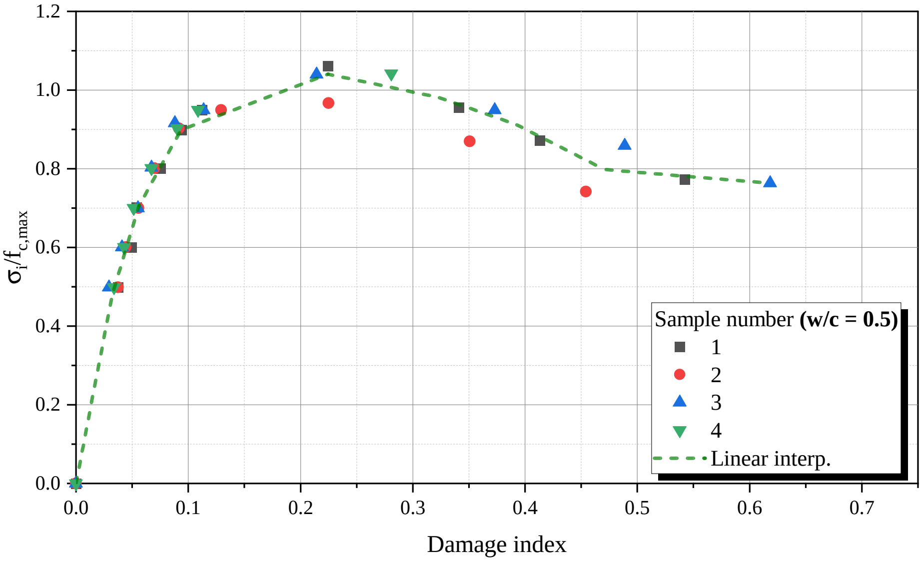

Figure 14. Damage evolution—w/c = 0.5.

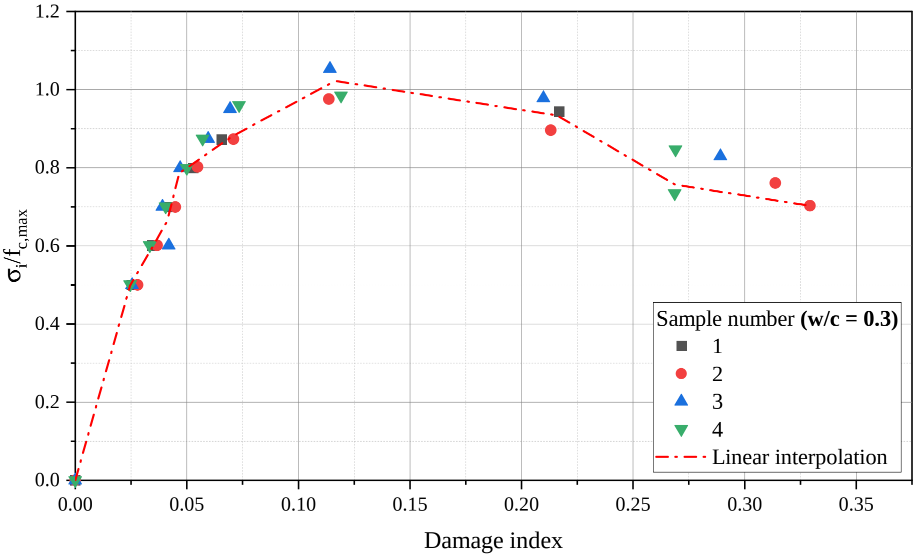

Figure 15. Damage evolution—w/c = 0.3.

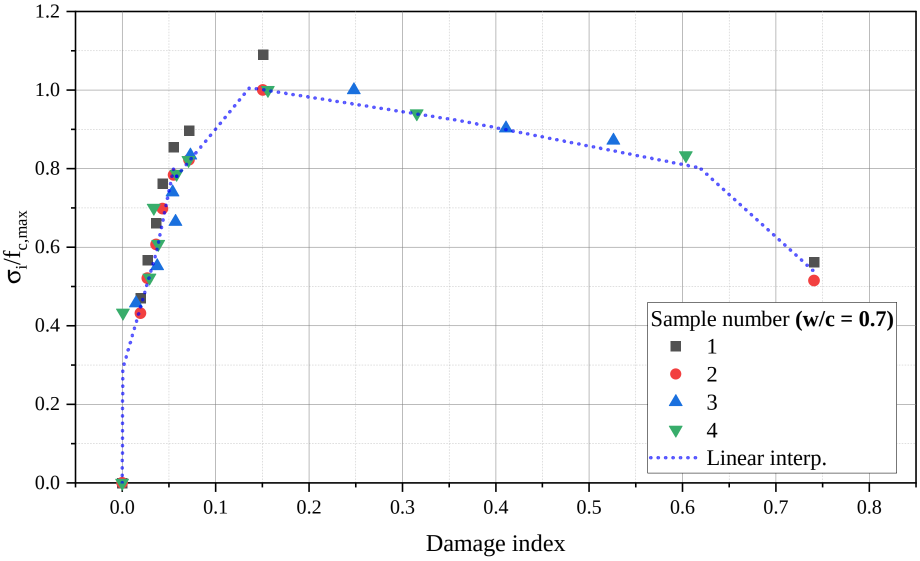

Figure 16. Damage evolution—w/c = 0.7.

Figure 17 shows that the concrete mixtures with w/c = 0.7 exhibit an increase in internal damping from $\xi_0 = 0.5\%$ (undamaged sample) to $\xi_{D=80\%} = 2.5\%$ (damage level of 0.8). Figure 18 illustrates the progression for a w/c = 0.5 mixture, with the internal damping ratio rising from $\xi_0 = 0.35\%$ to $\xi_{D=61\%} = 1.80\%$. Figure 19 depicts the evolution of damage and internal damping ratio for a w/c = 0.3 mixture, showing an increase in the internal damping ratio from $\xi_0 = 0.29\%$ to $\xi_{D=32\%} = 0.93\%$.

As the material progressively becomes damaged, there is an increase in the Coulomb damping component and additional vibration energy dissipation caused by the cracking. This leads to a higher internal damping ratio. Although the phenomenon is akin to three mixtures, it occurs at different scales.

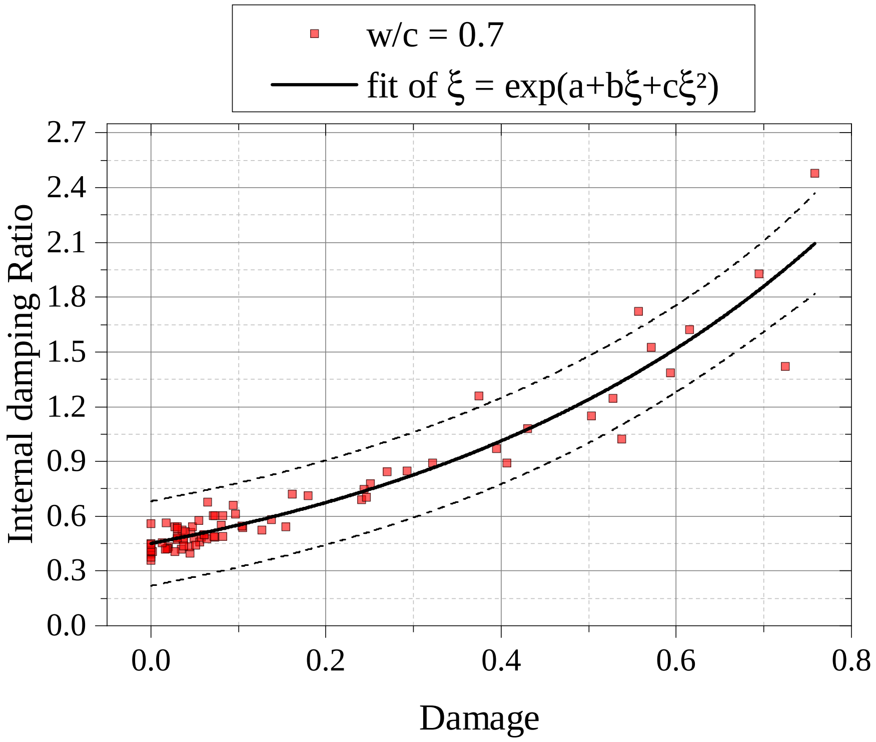

Figure 17. Influence of damage on internal damping ratio (w/c = 0.7).

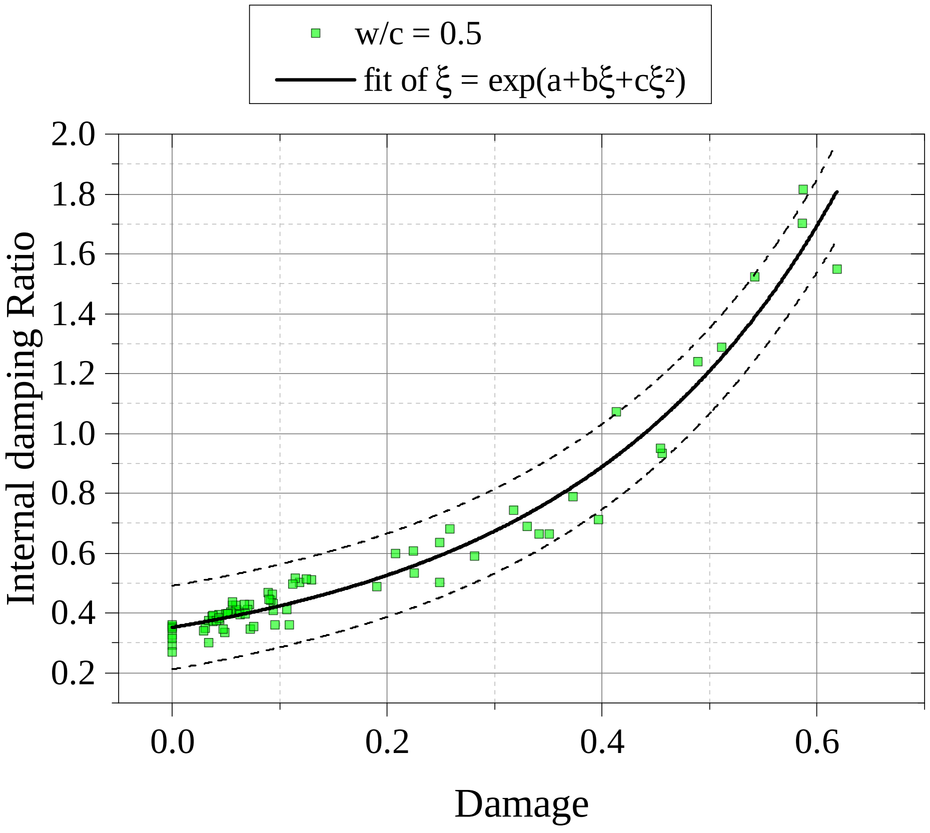

Figure 18. Influence of damage on internal damping ratio (w/c = 0.5).

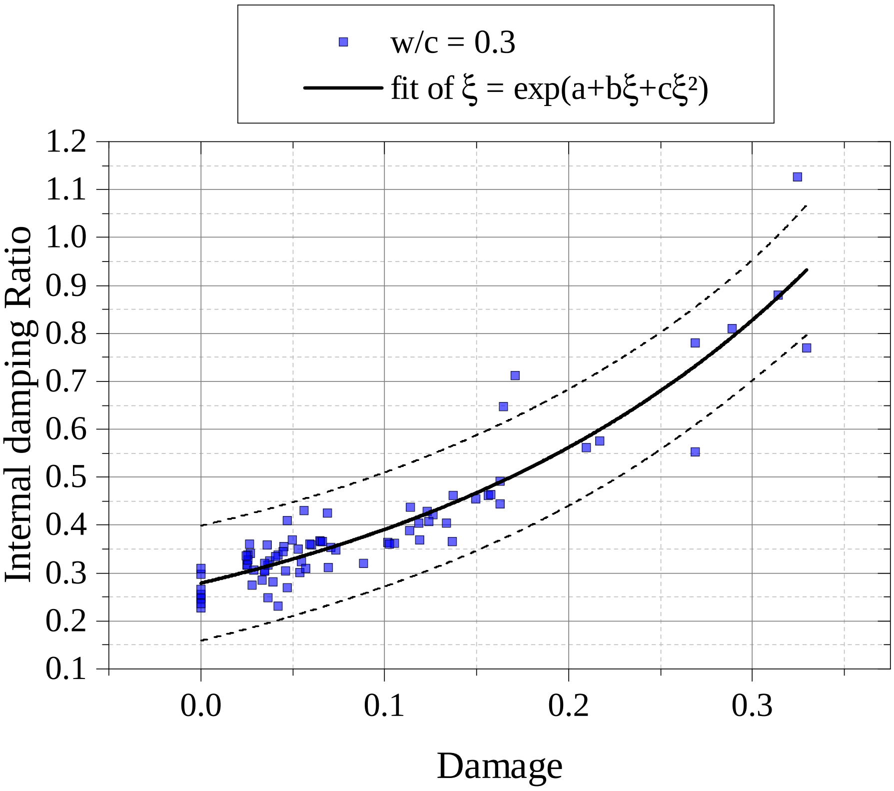

Figure 19. Influence of damage on internal damping ratio (w/c = 0.3).

4. Conclusions

This study advances on the internal damping ratio of concrete specimens under damage evolution using acoustic tests to assess the degradation of the dynamic elastic modulus and its impact on internal damping. The results can be input into numerical dynamic models that consider damage evolution and the increase in the internal damping ratio, especially for impact scenarios. The key findings include the following:

- The internal damping ratio is correlated with the water–cement (w/c) ratio, maturity, and dynamic modulus of elasticity. As the maturity increases, pore closure reduces viscous damping. C-S-H hydration reactions increase the material density, reducing internal dissipation and acoustic wave attenuation.
- Damage affects the damping ratio by increasing the Coulomb damping component, which improves internal damping. This phenomenon was observed for both the NSC and HSC mixtures at different scales.
- Microstructural factors, such as the initial porosity, early microcracking, and the transition zone, significantly affect the damage response and internal damping evolution. Higher w/c ratios lead to greater damage and higher internal damping and acoustic wave dissipation.
- The internal damping ratio is sensitive to microstructural changes and is closely related to damage progression.
- Few studies have quantified and understood internal damping under cyclic loading damage. This approach improves our understanding of concrete behaviour under dynamic excitation, particularly in impact scenarios.

Future research should address the variability introduced by different manual impacts. The standardisation of impacts will improve the consistency and accuracy of results. In addition, factors such as the moisture content and support conditions that affect internal damping should be considered. Implementing internal damping in a nonlinear constitutive model within the finite element method (FEM) would improve dynamic simulations.

Author Contributions: Methodology, G.d.M.S.G., P.A.K. and G.T.d.S.L.; Software, P.A.K.; Validation, P.A.K.; Formal analysis, R.M.B.; Investigation, G.d.M.S.G., R.M.B. and L.S.; Resources, R.M.B., L.S., R.S.R., G.T.d.S.L. and R.C.; Data curation, L.S.; Writing—original draft, G.d.M.S.G. and L.S.; Writing—review & editing, G.d.M.S.G., L.S., G.T.d.S.L. and R.C.; Visualization, R.S.R.; Supervision, G.T.d.S.L.; Project administration, R.S.R. and R.C.; Funding acquisition, R.C. All authors have read and agreed to the published version of the manuscript.

Funding: This study was financed in part by the Coordenação de Aperfeiçoamento de Pessoal de Nível Superior—Brasil (CAPES)—Finance Code 001 and by the National Council for Scientific and Technological Development (CNPq). Araucária Foundation-NAPI Wood-tech.

Data Availability Statement: The original contributions presented in the study are included in the article, further inquiries can be directed to the corresponding authors.

Conflicts of Interest: The authors declare no conflict of interest.

References

1. Paultre, P. *Dynamics of Structures*; ISTE ltd.: London, UK; Wiley: Hoboken, NJ, USA, 2011.
2. Chopra, A.K. *Dynamics of Structures: Theory and Applications to Earthquake Engineering*; Prentice Hall: Hoboken, NJ, USA, 2017.
3. Ewins, D.J. *Modal Testing: Theory, Practice and Application*; Research Studies Press: Brookline, MA, USA, 2000.
4. Chambreuil, C.; Giry, C.; Ragueneau, F.; Léger, P. Identification methods of material-based damping for cracked reinforced concrete beam models. *Earthq. Eng. Struct. Dyn.* **2023**, *52*, 2156–2178. [CrossRef]
5. Bachmann, H.; Ammann, W.J.; Eisenmann, J.; Floegl, I.; Hirsch, G.H.; Klein, G.K.; Lande, G.J.; Mahrenholtz, O.; Natke, H.G.; Nussbaumer, H.; et al. Vibration Problems in Structures-Practical Guidelines; Springer Science & Business Media: Berlin/Heidelberg, Germany, 1995.
6. Sugimoto, K.; Sugimoto, T.; Utagawa, N.; Kuroda, C.; Kawakami, A. Detection of internal defects of concrete structures based on statistical evaluation of healthy part of concrete by the noncontact acoustic inspection method. *Jpn. J. Appl. Phys.* **2018**, *57*, 07LC13. [CrossRef]
7. Zahedi, A.; Saliba, L.; Sanchez, L.F.M.; Boyd, A.J. Reliability of the Damage Rating Index to Assess Condition of Concrete Affected by External Sulfate Attack. *Mag. Concr. Res.* **2022**, *75*, 135–148. [CrossRef]
8. Smirnov, V.A.; Smolyakov, M. Experimental method for structural concrete damping properties evaluation. *Int. J. Comput. Civ. Struct. Eng.* **2022**, *18*, 14–22. [CrossRef]
9. Boccaccini, D.N.; Romagnoli, M.; Kamseu, E.; Veronesi, P.; Leonelli, C.; Pellacani, G.C. Determination of thermal shock resistance in refractory materials by ultrasonic pulse velocity measurement. *J. Eur. Ceram. Soc.* **2007**, *27*, 1859–1863. [CrossRef]
10. Pereira, A.H.; Fortes, G.M.; Schickle, B.; Tonnesen, T.; Musolino, B.; Maciel, C.D.; Rodrigues, J.A. Correlation between changes in mechanical strength and damping of a high alumina refractory castable progressively damaged by thermal shock. *Ceramica* **2010**, *56*, 311–314. [CrossRef]
11. Curadelli, R.O.; Riera, J.D.; Ambrosini, D.; Amani, M.G. Damage detection by means of structural damping identification. *Eng. Struct.* **2008**, *30*, 3497–3504. [CrossRef]
12. Pavese, A. Damping Estimation in Concrete Structures. *Struct. Health Monit.* **2014**, *13*, 1051–1063.
13. Salzmann, A. Damping Characteristics of Reinforced and Prestressed Normal-and High-Strength Concrete Beams. Ph.D. Thesis, Griffith University-Gold Coast Campus, Southport, Australia, 2002.
14. Salzmann, A.; Fragomeni, S.; Loo, Y.C. The Damping Analysis of Experimental Concrete Beams under Free-Vibration. *Adv. Struct. Eng.* **2003**, *6*, 53–64. [CrossRef]
15. Jordan, R.W. The effect of stress, frequency, curing, mix and age upon the damping of concrete. *MAgazine Concr. Res.* **1980**, *32*, 195–205. [CrossRef]
16. Kovacs, T. Microstructural Effects on Damping in Concrete. *Cem. Concr. Compos.* **2002**, *24*, 125–132.
17. Pyeon, S.; Kim, G.; Lee, S.; Nam, J. Internal Curing Effect of Waste Glass Beads on High-Strength Cement Composites. *Appl. Sci.* **2022**, *12*, 8385. [CrossRef]
18. Liu, K.; Long, Y.; Chen, L.; Ling, X.; Yu, R.; Shui, Z.; Fei, S.; Yu, W.; Li, C.; Ge, K. Mechanisms of autogenous shrinkage for Ultra-High Performance Concrete (UHPC) prepared with pre-wet porous fine aggregate (PFA). *J. Build. Eng.* **2022**, *54*, 104622. [CrossRef]
19. Gheorghiu, C.; Rhazi, J.E.; Labossiere, P. Impact resonance method for fatigue damage detection in reinforced concrete beams with carbon fibre reinforced polymer. *Can. J. Civ. Eng.* **2005**, *32*, 1093–1102. [CrossRef]
20. Ndambi, J.M.; Vantomme, J.; Harri, K. Damage assessment in reinforced concrete beams using eigenfrequencies and mode shape derivatives. *Eng. Struct.* **2002**, *24*, 501–515. [CrossRef]
21. Hosseinzadehfard, E.; Mobaraki, B. Investigating concrete durability: The impact of natural pozzolan as a partial substitute for microsilica in concrete mixtures. *Constr. Build. Mater.* **2024**, *419*, 135491. [CrossRef]
22. Bawa, N.; Graft-Johnson, J. Effect of Mix Proportion, Water-Cement Ratio, Age and Curing Conditions on the Dynamic Modulus of Elasticity of Concrete. *Build. Sci.* **1969**, *3*, 171–177.

23. Swamy, R. Damping Mechanisms in Cementitious Systems. In Proceedings of the Conference on Dynamic Waves in Civil Engineering, Swansea, UK, 7–9 July 1970; pp. 521–542.
24. Eiras, J. Microstructural Influences on Damping in Concrete. *J. Mater. Sci.* **2015**, *50*, 2345–2356.
25. Gidrão, G.d.M.S.; Krahl, P.A.; Carrazedo, R. Internal damping ratio of Ultra-High-Performance Fiber-Reinforcement Concrete (UHPFRC) considering the effect of fiber content and damage evolution. *J. Mater. Civ. Eng.* **2020**, *32*. [CrossRef]
26. Haug, K. Cracking Effects on Damping in Concrete. *Mater. Struct.* **2018**, *51*, 234–245.
27. Swamy, N.; Rigby, G. Dynamic properties of hardened paste, mortar and concrete. *Matériaux Constr.* **1971**, *4*, 13–40. [CrossRef]
28. Swamy, R.N. Dynamic Poisson's Ratio of Portland Cement Paste, Mortar and Concrete. *Cem. Concr. Res.* **1971**, *1*, 559–583. [CrossRef]
29. Tian, Y.; Lu, D.; Zhou, J.; Yang, Y.; Wang, Z. Damping Property of Cement Mortar Incorporating Damping Aggregate Yaogang. *Materials* **2020**, *13*, 792. [CrossRef] [PubMed]
30. Tian, Y.; Yan, X.; Zhang, M.; Yang, T.; Zhang, J.; Wang, Z. Effect of the characteristics of lightweight aggregates presaturated polymer emulsion on the mechanical and damping properties of concrete. *Constr. Build. Mater.* **2020**, *253*, 119154. [CrossRef]
31. Li, N.; Long, G.; Fu, Q.; Wang, X.; Ma, K.; Xie, Y. Effects of freeze and cyclic flexural load on mechanical evolution of filling layer self-compacting concrete. *Constr. Build. Mater.* **2019**, *200*, 198–208. [CrossRef]
32. Seracino, R. Damping in Concrete with Rubber Additives. *Constr. Build. Mater.* **2007**, *21*, 123–132. [CrossRef]
33. Wang, X.; Zhou, C. Numerical investigation for the flexural strengthening of reinforced concrete beams with external prestressed HFRP sheets. *Constr. Build. Mater.* **2018**, *189*, 804–815. [CrossRef]
34. *ASTM C150-04*; Standard Specification for Portland Cement. ASTM: West Conshohocken, PA, USA, 2011; Volume 4, pp. 1–7.
35. *ABNT NBR 7211*; Agregados para Concreto-Especificação. ABNT: Rio de Janeiro, Brazil, 2009.
36. *ASTM C215-02*; Standard Test Method for Fundamental Transverse, Longitudinal, and Torsional Resonant Frequencies of Concrete Specimens. ASTM: West Conshohocken, PA, USA, 2003; pp. 1–7.
37. *ASTM E1876-01*; Standard Test Method for Dynamic Young's Modulus, Shear Modulus, and Poisson's Ratio by Impulse Excitation of Vibration. ASTM: West Conshohocken, PA, USA, 2001.
38. Krahl, P.A.; Gidrão, G.D.M.S.; Carrazedo, R. Compressive behavior of UHPFRC under quasi-static and seismic strain rates considering the effect of fiber content. *Constr. Build. Mater.* **2018**, *188*, 633–644. [CrossRef]
39. Krahl, P.A.; Gidrão, G.d.M.S.; Carrazedo, R. Cyclic behavior of UHPFRC under compression. *Cem. Concr. Compos.* **2019**, *104*, 103363. [CrossRef]
40. Haach, V.G.; Carrazedo, R.; Oliveira, L.M.; Corrêa, M.R. Application of acoustic tests to mechanical characterization of masonry mortars. *NDT E Int.* **2013**, *59*, 18–24. [CrossRef]
41. Pickett, G. Equations for Computing Elastic Constants from Flexural and Torsional Resonant Frequencies of Vibration of Prisms and Cylinders. *Proc. Am. Soc. Test. Mater.* **1945**, *45*, 846–866.
42. Pereira, A.H.A.; Otani, L.B.; De Anchieta Rodrigues, J.; Traon, N.; Tonnesen, T.; Telle, R. The influence of nonlinear elasticity on the accuracy of thermal shock damage evaluation by the impulse excitation technique. *InterCeram Int. Ceram. Rev.* **2011**, 98–102.
43. Pereira, A.H.A.; Musolino, B.; Maciel, C.D.; Rodrigues, J.A. Algorithm to determine the damping of ceramic materials by the impulse excitation technique ceramic materials by the impulse excitation technique. *Ceramica* **2012**, *58*, 229–237. [CrossRef]